



Piezoelectric energy harvesting from vortex-induced vibrations of circular cylinder

A. Mehmood^a, A. Abdelkefi^a, M.R. Hajj^{a,*}, A.H. Nayfeh^a, I. Akhtar^b, A.O. Nuhait^c

^a Department of Engineering Science and Mechanics, MC 0219, Virginia Polytechnic Institute and State University, Blacksburg, VA 24061, USA

^b Department of Mechanical Engineering, NUST College of Electrical & Mechanical Engineering, National University of Sciences & Technology, Islamabad, Pakistan

^c Department of Mechanical Engineering, King Saud University, Riyadh 11421, Saudi Arabia

ARTICLE INFO

Article history:

Received 10 September 2012

Received in revised form

16 March 2013

Accepted 19 March 2013

Handling Editor: M.P. Cartmell

Available online 7 May 2013

ABSTRACT

The concept of harvesting energy from a circular cylinder undergoing vortex-induced vibrations is investigated. The energy is harvested by attaching a piezoelectric transducer to the transverse degree of freedom. Numerical simulations are performed for Reynolds numbers (Re) in the range $96 \leq Re \leq 118$, which covers the pre-synchronization, synchronization, and post-synchronization regimes. Load resistances (R) in the range $500 \Omega \leq R \leq 5 \text{ M}\Omega$ are considered. The results show that the load resistance has a significant effect on the oscillation amplitude, lift coefficient, voltage output, and harvested power. The results also show that the synchronization region widens when the load resistance increases. It is also found that there is an optimum value of the load resistance for which the harvested power is maximum. This optimum value does not correspond to the case of largest oscillations, which points to the need for a coupled analysis as performed here.

© 2013 Elsevier Ltd. All rights reserved.

1. Introduction

Converting ambient and aeroelastic vibrations to a usable form of electric power has been proposed for powering electronic components, such as microelectromechanical systems, actuators [1,2], and health monitoring wireless sensors [3–5], or for replacing small batteries that have a finite life span or would require hard and expensive maintenance [6,7]. Different transduction mechanisms can be employed for converting these vibrations to electric power, including electrostatic [8,9], electromagnetic [10], and piezoelectric [10,11] transduction. Of particular interest is the piezoelectric option, which has received the most attention because it can be used to harvest energy over a wide range of frequencies [9] and can be easily implemented. To date, most of energy harvesting from mechanical vibrations has concentrated on exploiting base excitations [12–16]. More recently, there has been several investigations into the conversion of aeroelastic vibrations into electric power [17–26].

The flow past a vibrating cylinder is a canonical problem that has been investigated to understand various flow physics phenomena. When a fluid passes over a cylinder, an organized and periodic array of concentrated vorticity, known as the von Kármán vortex street, appears in the wake. For stationary cylinders, the vortex-shedding frequency f_{vs} is usually expressed as a nondimensional frequency, called the Strouhal number $St = f_{vs}D/U_{\infty}$, where U_{∞} and D are, respectively, the

* Corresponding author. Tel.: +1 5402314190; fax: +1 5402314574.

E-mail address: mhajj@vt.edu (M.R. Hajj).

incoming free-stream velocity and the diameter of the cylinder. If the cylinder is allowed to flex or move rigidly, these forces may cause it to oscillate; a phenomenon that is usually referred to as vortex-induced vibration (VIV). In cases where the vortices are shed at a frequency near the natural frequency of the cylinder, it undergoes high-amplitude oscillations. This phenomenon is called “lock-in” or “synchronization”. In this work, the regimes before and after such synchronization takes place are, respectively, referred to as pre-synchronous and post-synchronous regimes. For a comprehensive review of the VIV phenomenon of circular cylinders, the reader is referred to Refs. [27–30].

To accurately determine the level of harvested power from vortex-induced vibrations of circular cylinders, one needs to consider the tight coupling between the mechanical and electrical components of the harvester. This can only be achieved by simultaneously solving the governing equations. In this work, we consider the flow, cylinder's motion and electrical transduction as one single dynamical system. We then perform tightly coupled simulations to determine the level of harvested power from this system under different operating conditions including the Reynolds number and load resistance. The focus is on the synchronization region where the oscillation amplitudes remain very high. In Section 2, we discuss the fluid flow solver, piezoaeroelastic modeling and the coupling scheme. In Section 3, validation of the fluid flow solver and the coupling scheme with previous experimental and numerical results is presented. In Section 4, the effects of the load resistance on the electromechanical damping and the global natural frequency are discussed. In Section 5, the effects of the Reynolds number and the load resistance on the oscillation amplitude, fluctuating lift coefficient, voltage output, and harvested power are discussed. The conclusions are presented in Section 6.

2. Mathematical modeling and numerical simulations

2.1. Fluid flow solver

The numerical simulations of the equations governing the interaction of a flow with a freely oscillating cylinder are very challenging. The challenge arises because the boundary conditions change as the cylinder moves. Different formulations have been proposed and developed including the immersed boundary (IB) [31], arbitrary Lagrangian–Eulerian (ALE) [32], and accelerating reference frame (ARF) [33] methods. In this work, we use a parallel CFD code [34,35], in which the incompressible continuity and unsteady Navier–Stokes equations are solved using an accelerated reference frame (ARF) technique. In this technique, the momentum equation is directly coupled with the cylinder motion by adding a reference frame acceleration term [33,34]; the outer boundary conditions of the flow domain are then updated using the response of the cylinder. Note that, in the implemented scheme, the fluid, the cylinder and piezoelectric are considered as elements of a single dynamical system, and all the governing equations are solved simultaneously. The governing equations of the fluid flow are given by

$$\frac{\partial u_j}{\partial x_j} = 0 \quad (1)$$

$$\frac{\partial u_i}{\partial t} + \frac{\partial}{\partial x_j} (u_j u_i) = -\frac{\partial p}{\rho \partial x_i} + \nu \frac{\partial^2 u_i}{\partial x_j \partial x_j} - \ddot{x}_i, \quad (2)$$

where $i, j = 1, 2, 3$, u_i represent the Cartesian velocity components (u, v, w), ρ , p and ν are the density, pressure and kinematic viscosity of the fluid, respectively. Here, $\ddot{x}_i = a$ is used to denote the cylinder acceleration in the cross-flow direction. In the implemented flow solver, the governing equations are nondimensionalized using the cylinder diameter D as a reference length and the incoming free-stream velocity U_∞ as a reference velocity. The Reynolds number is defined as $Re = U_\infty D / \nu$.

At the domain boundary, the velocity boundary condition is modified to include the effect of the moving cylinder; that is,

$$\mathbf{u} = \mathbf{u}_D - \mathbf{v}, \quad (3)$$

where \mathbf{u}_D is the velocity in the inertial frame of reference and $\mathbf{v} = \dot{\mathbf{x}}$ is the cylinder velocity. On the cylinder surface, the velocity boundary condition is $u_i = 0$. The pressure boundary condition is obtained by dotting the domain unit outward normal \mathbf{n} with Eq. (2) and using the vector identity $\nabla^2 \mathbf{u} = \nabla(\nabla \cdot \mathbf{u} - \nabla \times \nabla \times \mathbf{u})$. The result is

$$\frac{\partial p}{\partial n} = \rho \mathbf{n} \cdot \left[(\mathbf{u} \cdot \nabla) \mathbf{u} - \nu \nabla \times \nabla \times \mathbf{u} - \ddot{\mathbf{x}} - \frac{\partial \mathbf{u}}{\partial t} \right] \quad (4)$$

On the far-field boundary, $\partial u_i / \partial t = -\ddot{x}_i$, whereas on the cylinder surface $\partial u_i / \partial t = 0$.

The shed vortices generate a time-varying fluid force on the cylinder surface in the cross-stream direction that causes the vortex-induced vibrations. In our CFD code, this force is computed from the surface pressure as

$$C_L = - \int_0^{2\pi} \left(p \sin \theta - \frac{1}{Re} \omega_z \cos \theta \right) d\theta, \quad (5)$$

where ω_z is the spanwise vorticity component on the cylinder surface and θ is the angle that the outer normal of the area component makes with the flow direction. As shown in Fig. 1, a body conformal “O”-type grid is employed to simulate the flow over the cylinder. We employ curvilinear coordinates (ξ, η, ζ) in an Eulerian reference frame. For the specific case of

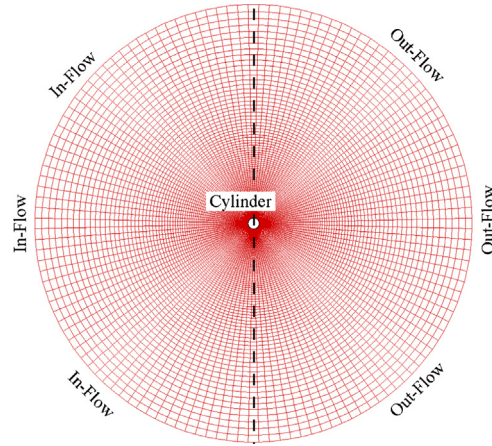


Fig. 1. A two-dimensional layout of an "O"-type grid in the (r, θ) -plane.

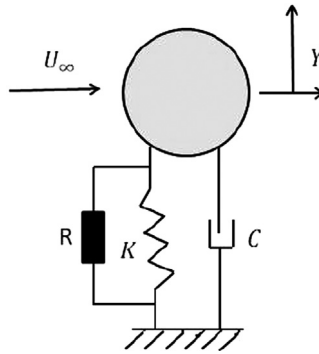


Fig. 2. A schematic of the proposed cylinder-based piezoaeroelastic energy harvester, where U_∞ is the free stream velocity, C and K represent the structural damping and stiffness, respectively, and R is the electrical load resistance.

a circular cylinder, the generalized coordinates (ξ, η, ζ) can be represented by polar coordinates (r, θ, z) . Details of the numerical discretization and the parallel implementation can be found in Refs. [34–36].

2.2. Representation and modeling of the piezoaeroelastic system

The energy harvester under investigation consists of an elastically mounted rigid cylinder, which undergoes vortex-induced vibrations in the transverse direction when subjected to an incoming flow; as shown in the schematic presented in Fig. 2. Including the piezoelectric transducer and considering a load resistance in the electrical circuit [40,41,26], we add to the flow equations, the equations governing the cylinder displacement, Y , and generated voltage, V , which are written as

$$M\ddot{Y} + C\dot{Y} + KY - \theta V = F_Y(t), \quad (6)$$

$$C_p \dot{V} + \frac{V}{R} + \theta \dot{Y} = 0 \quad (7)$$

where M is the mass of the oscillating cylinder per unit length, C and K are used to represent the structural damping and stiffness, respectively, $F_Y(t)$ characterizes the time-dependent excitation of the fluid flow applied on the structure, R is the electrical load resistance, V is the voltage across this load resistance, C_p is the capacitance of the piezoelectric layer, and θ is the electromechanical coupling term. To assess the physics of this system, we consider as an example, a system that has geometric and material properties as presented in Table 1. The geometric and material properties of the cylinder are the same as in the experiments of Anagnostopoulos and Bearman [42] which is used to validate the flow solver.

Table 1
Properties of the coupled system.

Physical parameters	Values
Mass of the cylinder per unit length (M) [kg]	0.2979
Diameter (D) [mm]	1.6
Stiffness per unit length (K) [N/m]	579
Damping per unit length (C) [N s/m]	0.0325
Damping ratio (ζ)	0.0012
Mass ratio (m^*)	149.1
Cylinder oscillation frequency (f_c) [Hz]	7.016
Capacitance (C_p) [nF]	120
Electromechanical coupling (θ) [N/V]	1.55×10^{-3}

2.3. Nondimensionalization and coupling of the piezoaeroelastic system

To generalize and solve the coupled problem, we use the diameter of the cylinder D and the incoming free-stream velocity U_∞ as the length and velocity scales. We then rewrite Eqs. (6) and (7) in nondimensional form as

$$\ddot{Y}^* + \left(\frac{4\pi\zeta}{U_r}\right) \dot{Y}^* + \left(\frac{2\pi}{U_r}\right)^2 Y^* - \left(\frac{1}{U_r}\right)^2 V^* = \frac{2}{\pi m^*} C_L, \quad (8)$$

$$\dot{V}^* + \sigma_1 \dot{Y}^* + \frac{\sigma_2}{U_r} V^* = 0 \quad (9)$$

where $Y^* = Y/D$ is the nondimensional transverse cylinder displacement, $U_r = U_\infty/f_c D$ is the reduced velocity, $\zeta = C/C_{\text{crit}} = C/2\sqrt{KM}$ is the structural damping ratio, $m^* = M/M_f$ is the mass ratio, $M_f = \frac{1}{4}\rho\pi D^2$ represents the fluid mass per unit length displaced by the cylinder, $V^* = V/V_o$, $V_o = Mf_c^2 D/\theta$, $\sigma_1 = \theta^2/MC_p f_c^2$, $\sigma_2 = 1/RC_p f_c$, and f_c is the natural vibration frequency of the rigid cylinder.

The governing electromechanical equations (8) and (9) can be written as a coupled system of three first-order ordinary-differential equations as

$$y_1 = y_2 \quad (10)$$

$$\dot{y}_2 = -\left(\frac{2\pi}{U_r}\right)^2 y_1 - \frac{4\pi\zeta}{U_r} y_2 + \frac{1}{U_r^2} y_3 + \frac{2}{\pi m^*} C_L \quad (11)$$

$$\dot{y}_3 = -\sigma_1 y_2 - \frac{\sigma_2}{U_r} y_3 \quad (12)$$

where $y_1 = Y^*$, $y_2 = \dot{Y}^*$ and $y_3 = V^*$.

2.4. Coupling scheme

Numerical simulation of energy harvesting from the vortex-induced vibrations is very challenging as one cannot solve for the motion of the cylinder and the generated voltage from the load resistance without determining the fluid loads. Yet, one cannot determine the fluid loads without the knowledge of the motion of the cylinder and the effects of energy harvesting on this motion. This complication necessitates that Eqs. (1) and (2), which govern the dynamics of the flow field, and Eqs. (8) and (9), which govern the dynamics of the cylinder and generated voltage, be solved in a coupled manner. To overcome this difficulty, we use the Hamming fourth-order predictor–corrector technique [39]. In this technique, the fluid loads (output of the CFD code) are coupled to ODEs governing the cylinder's motion and harvested voltage. The predicted state of the cylinder, which depends on the load resistance, is then used in the CFD code to compute the new fluid loads. These loads are then used to compute the new states of the cylinder and voltage using the corrector scheme. The above steps are repeated until a match between the fluid loads and the cylinder's motion, as defined by a specified conditional error at each time step is reached. The Hamming's fourth-order predictor–corrector algorithm requires the solutions at three previous time steps to compute the solutions (loads and cylinder motion) at the current time step. For the first time step, Euler and modified Euler methods are used, then Adams–Bashforth two-step predictor and Adams–Moulton two-step corrector schemes are used for second time step and Adams–Bashforth three-step predictor and Adams–Moulton three-step corrector schemes are used for the third time step.

To describe the numerical procedure of solving the equations of motion, we represent Eqs. (10)–(12) as

$$\dot{y}_t = f(t, y_1(t), y_2(t), y_3(t)) \quad (13)$$

1. The right-hand side of Eq. (13) is evaluated at the present time step $t \geq 4$, knowing the solution at the three previous time steps and the solution is computed using Hamming's predictor as

$$y_t^p = y_{t-4} + \frac{4\Delta t}{3}(2f_{t-1} - f_{t-2} + 2f_{t-3}) \quad (14)$$

2. The predicted solutions, y_t^p , are modified by using the truncation-error estimates from the previous time step ($t-1$) as

$${}^{mp}y_t = y_t^p + \frac{112}{9}e_{t-1} \quad (15)$$

At this stage (end of predictor section), the response of the cylinder is found and is supplied to the fluid solver in order to compute the fluid loads at the new time step. Note that the fluid load is computed using the previous flow field with the new state (i.e., based on the predictor section) of the cylinder. The right-hand sides of Eq. (13) are re-evaluated at the current time step.

3. The modified-predicted solutions are corrected by using the Hamming's corrector equation

$${}^{k+1}y_t^c = \frac{1}{8}(9y_{t-1} - y_{t-3} + 3\Delta t({}^k f_t + 2f_{t-1} - f_{t-2})) \quad (16)$$

where

$${}^k f_t = f({}^k y_t) \quad (17)$$

and ${}^1y_t = y_t^{mp}$ where k is the iteration counter and is set equal to 1 at the beginning of the corrector scheme.

4. The iterations are stopped after either reaching the specified iterations or after convergence as

$$|{}^{k+1}y_t - {}^k y_t| \leq \epsilon \quad (18)$$

where ϵ is the user specified error.

5. After convergence of the solution, the truncation error te for use in the current and next time step is computed as

$$te = \frac{9}{121}({}^{k+1}y_t - {}^k y_t) \quad (19)$$

6. The corrected solutions, ${}^{k+1}y_t^c$, are modified by using the new truncation-error estimate, te , as

$$y_t = {}^{k+1}y_t^c - e_t \quad (20)$$

The procedure (1–6) is repeated to march in time. Further details of the numerical discretization, parallel implementation, and the coupling scheme can be found in Refs. [34,35,38,37]. The above overall coupling scheme has been summarized in the flow chart in Fig. 3.

3. Validation of the fluid flow solver and the coupling scheme

The fluid flow solver and the coupling scheme are validated by comparing the cylinder's displacement with experimental results of Anagnostopoulos and Bearman [42] and other numerical simulations performed by Yang et al. [43] and Schulz and Kallinderis [44]. We employ 192×256 grid points in the θ - and z -directions, respectively, with a computational domain of $25D$. We increase the Reynolds number with small increments from $Re = 94$ to $Re = 140$. This range corresponds to reduced velocities from $U_r = 5.23$ to $U_r = 7.79$. We note that the cylinder is allowed to move only in the transverse direction under the action of the fluid forces.

Fig. 4 shows the variation of the nondimensional maximum oscillation amplitude Y_{\max}/D of the cylinder as a function of the Reynolds number. From this plot, we note that we are able to obtain a better agreement of the location of the bifurcation point (onset of synchronization) with the experimental results than previously reported numerical simulations [43,44]. Still, there is a small difference between our simulations and the experimental data [42] when comparing the maximum amplitude and the range of the synchronization regime. This difference, which has been reported by the other numerical studies [43,44], could be due to the three-dimensional effects, since the experiments were performed without end plates.

4. Effect of the load resistance on the onset of synchronization

Adding a load resistance results in a variation of the natural frequency and damping of the coupled system. Because the onset of the synchronization region is defined by matching the natural frequency of the coupled electromechanical system

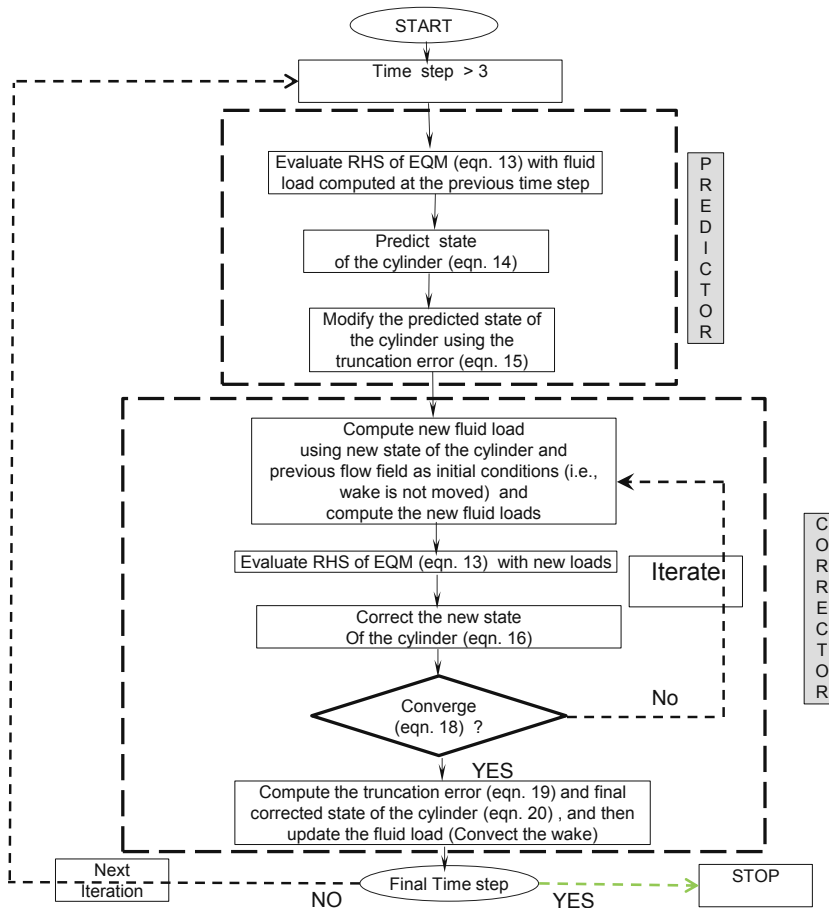


Fig. 3. Layout of predictor–corrector scheme.

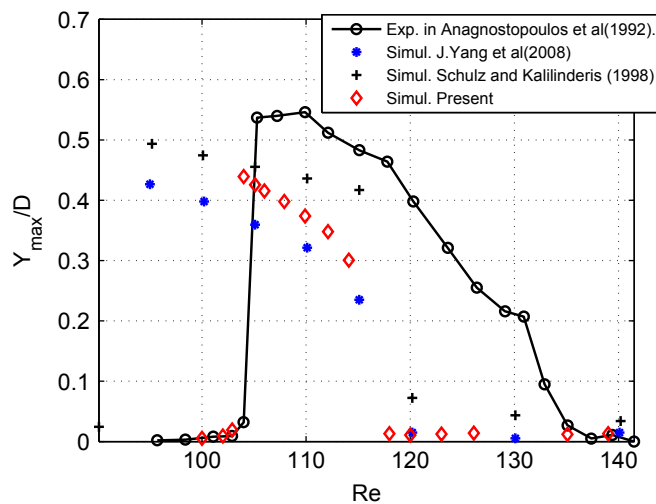


Fig. 4. Comparison of maximum displacement amplitudes as predicted in present computations (\diamond) with the experimental measurements of [42] (\circ) and numerical computations of [43] ($*$) and [44] (+). (For interpretation of the references to color in this figure caption, the reader is referred to the web version of this article.)

with the frequency of the vortex-induced vibration, we perform, as a first step, a linear analysis to determine the variations in the natural frequency and damping that are due to adding the load resistance. As such, we consider the electromechanical governing equations of the cylinder, which are rewritten as

$$M\ddot{Y} + C\dot{Y} + KY - \theta V = 0 \quad (21)$$

$$C_p\dot{V} + \frac{V}{R} + \theta\dot{Y} = 0 \quad (22)$$

we rewrite Eqs. (21) and (22) as the following set of first-order differential equations:

$$\dot{X}_1 = X_2, \quad (23)$$

$$\dot{X}_2 = -(2\pi f_c)^2 X_1 - 4\pi f_c \zeta X_2 + \frac{\theta}{M} X_3, \quad (24)$$

$$\dot{X}_3 = -\frac{\theta}{C_p} X_2 - \frac{1}{C_p R} X_3 \quad (25)$$

where $X_1 = Y$, $X_2 = \dot{Y}$ and $X_3 = V$.

Eqs. (23)–(25) can be expressed in vector form as

$$\dot{\mathbf{X}} = \mathbf{A}(R)\mathbf{X} \quad (26)$$

where

$$\mathbf{A}(R) = \begin{pmatrix} 0 & 1 & 0 \\ -(2\pi f_c)^2 & -4\pi f_c \zeta & \frac{\theta}{M} \\ 0 & -\frac{\theta}{C_p} & -\frac{1}{C_p R} \end{pmatrix}$$

and

$$\mathbf{X} = \begin{pmatrix} X_1 \\ X_2 \\ X_3 \end{pmatrix}$$

Variations of the real and imaginary parts of the eigenvalue k_i of the linear electromechanical coupled system are shown in Fig. 5. It is clear from Fig. 5(b) that, for the considered parameters of the coupled system, the global natural frequency remains almost constant, with a value near 44.05 rad/s, for small values of the load resistance $R < 30 \text{ k}\Omega$. This value of the global natural frequency ($R = 100 \Omega$) is referred as the short global frequency. For large values of R , the global natural frequency becomes equal to 44.8 rad/s. This value of the global natural frequency $R = 10 \text{ M}\Omega$ is referred to the open global frequency. The plot in Fig. 5(a) shows that the electromechanical damping remains very low for small values of the load resistance, increases to a maximum for load resistance values of nearly $200 \text{ k}\Omega$, and then decreases and remains low for larger values of the load resistance. This maximum value in the coupled electromechanical damping is due to the resistive shunt damping effect. This analysis shows that the load resistance impacts the natural frequency and damping of the coupled electromechanical system. The impact of these variations in both of the frequency and damping on the system outputs is discussed further in Section 5.2.

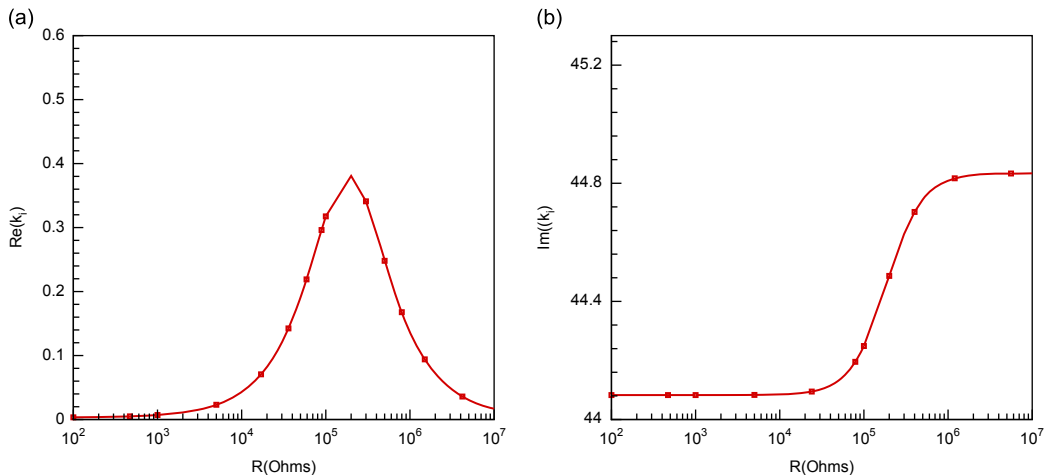


Fig. 5. Variation of the real k_r and imaginary k_i parts of the eigenvalue k of the linear system with the load resistance.

5. Results and discussion

5.1. Effect of Reynolds number on the system outputs

To investigate harvesting energy from the considered piezoaeroelastic system, we perform numerical simulations of the flow over a rigid cylinder that moves in the cross-flow direction and has a piezoelectric transducer attached to this direction. As the ultimate goal is to power small sensors and actuators, we limit this study to a Reynolds number in the range $96 \leq Re \leq 118$, which corresponds to a cylinder having a diameter ranging from 0.1 mm to 1.6 mm and placed in a water stream of $0.96 \text{ m/s} \leq U_\infty \leq 1.18 \text{ m/s}$ and/or $0.06 \text{ m/s} \leq U_\infty \leq 0.07375 \text{ m/s}$. This range corresponds to reduced velocities in the range $5.34 \leq U_r \leq 6.57$. Note that for all cases the flow over a stationary cylinder was initially computed for the same Reynolds number. Then, the cylinder was allowed to move and the frequency of vortex shedding (f_{vs}), the cylinder oscillation frequency, the voltage output, and the harvested power are recorded, after reaching steady state.

We conducted numerical simulations for a wide range of load resistances. The same tendency in the system outputs was observed over the whole range. To present the important physical observations, we consider the response of the cylinder and the level of generated voltage for $R = 5 \text{ k}\Omega$ while varying the Reynolds number. In Fig. 6, we show time histories of the cylinder displacement, lift coefficient, and associated voltage output for the pre-synchronous, synchronous, and post-synchronous regimes. In the pre-synchronous regime ($Re=96$), the cylinder oscillations remain very low ($Y/D \sim 10^{-3}$), as shown in Fig. 6(a). The lift coefficient, presented in Fig. 6(b), oscillates around a zero mean with a peak value of 0.325. The response in this regime is quasi-periodic consisting of two major frequencies, the shedding frequency and the cylinder

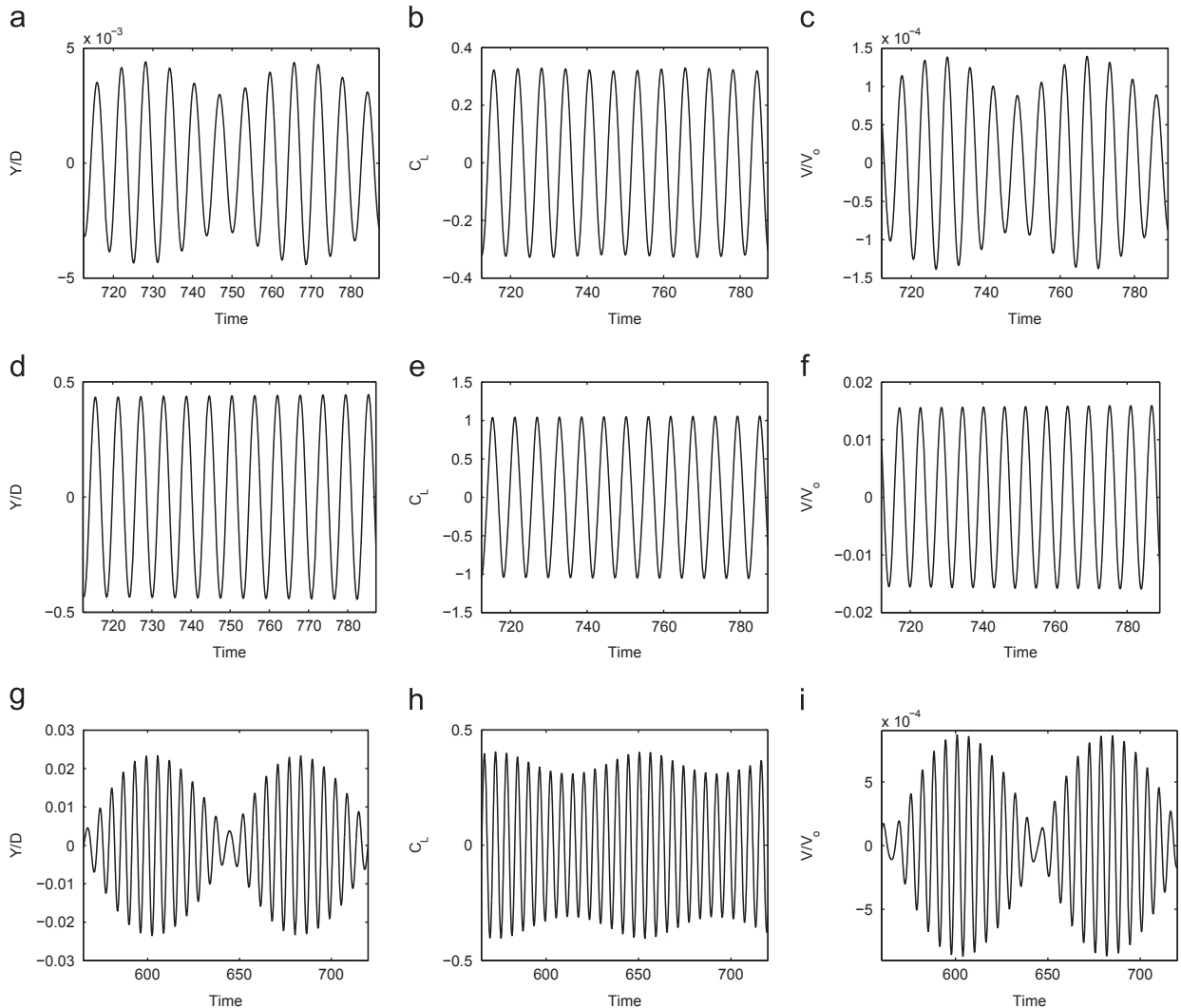


Fig. 6. Time histories of the transverse displacement, fluctuating lift coefficient, and voltage output for the pre-synchronous ($Re=96$) (a,b,c), synchronous ($Re=104$) (d,e,f), and post-synchronization ($Re=116$) (g,h,i) regimes, respectively, when the load resistance $R = 5 \text{ k}\Omega$.

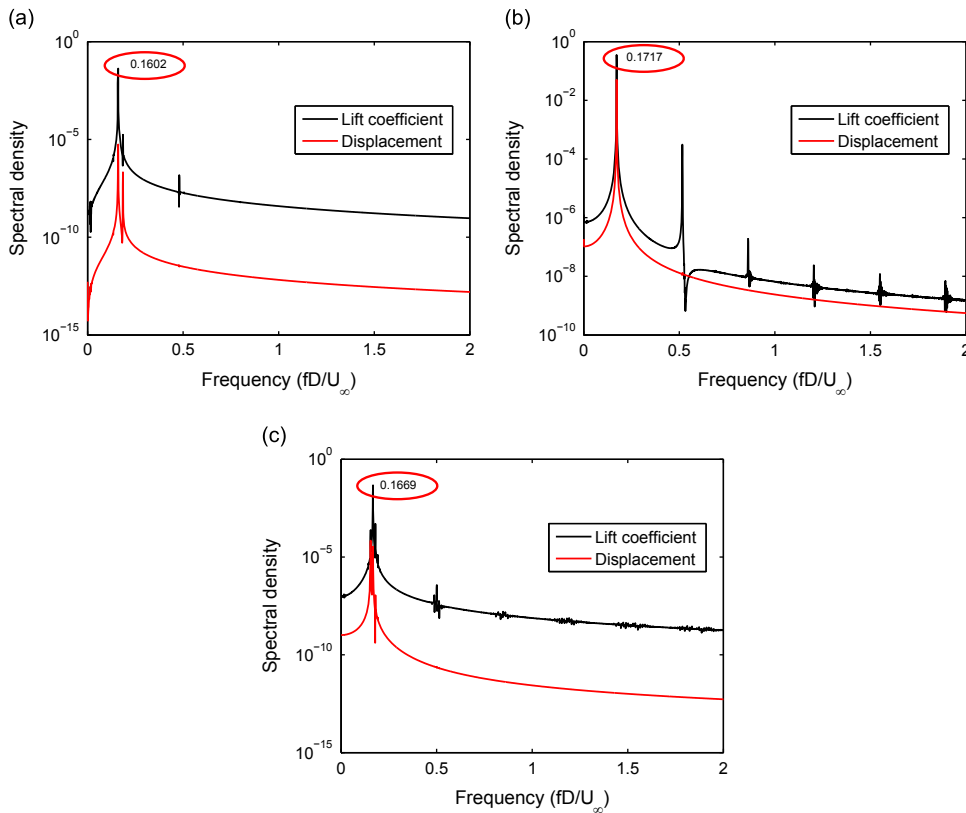


Fig. 7. Power spectra of (a) pre-synchronous, (b) synchronous, and (c) post-synchronous regimes for an oscillating cylinder in the cross-flow direction at the specified Reynolds number when $R = 5 \text{ k}\Omega$.

global frequency. The voltage output in Fig. 6(c) shows that, as expected, its time history follows very closely that of the displacement. Similar values for the displacement, lift, and voltage are observed for Reynolds numbers up to $Re = 104$. At $Re = 104$, high oscillation amplitudes of the cylinder are observed. Time histories of the cylinder displacement, lift coefficient, and voltage output at $Re = 104$ are shown in Fig. 6(d), (e), and (f), respectively. These plots show periodic responses with a dominant frequency, which is the cylinder natural frequency. These large oscillation amplitudes extend up to $Re = 114$. This is due to the fact that the range from $Re = 104$ to $Re = 114$ corresponds to the synchronization regime at $R = 5 \text{ k}\Omega$. At $Re = 116$, the synchronization phenomenon bifurcates, a high level of modulation is observed in the time histories of the displacement and voltage, as shown in Fig. 6(g) and (i). Modulations also exist in the time history of the lift coefficient presented in Fig. 6(h). For all considered cases, we note that the time histories of the transverse displacement and harvested voltage have the same trend. This is expected because the generated voltage is directly related to the transverse displacement through the Gauss law (Eq. (22)).

Further insight into the different aspects of the displacement and lift coefficient can be obtained from the power spectra of their time histories, as shown in Fig. 7. When $Re = 96$, in the pre-synchronous regime, Fig. 7(a) shows two spectral peaks: one peak at 0.1602, which is the vortex shedding frequency, and a smaller one at 0.185, which corresponds to the cylinder global natural frequency. Here, it can be inferred that the response is quasi-periodic and is not synchronized with the cylinder global frequency. In the synchronous regime ($Re = 104$), Fig. 7(b) shows that both of the lift and displacement have the same oscillation frequency. Moreover, the vortices are shed at the cylinder global natural frequency (i.e., $f_{vs} \cong f_c$), indicating that synchronization has taken place as the two frequencies have merged. In the post-synchronous regime, ($Re = 116$), Fig. 7(c) shows three dominant peaks: the vortex shedding frequency ($f_{vs} = 0.1669$) and two asymmetric sidebands, indicating an amplitude and phase modulated response.

5.2. Effect of the load resistance on the system outputs

Numerical simulations are performed for different values of the electrical load resistances over a range of Reynolds numbers that covers the pre-synchronous, synchronous, and post-synchronous regimes. Fig. 8(a) shows variations of the root mean square (rms) amplitudes of the cylinder oscillations with the Reynolds number and load resistance. The plot shows that the synchronization phenomenon starts for all load resistances at about the same Reynolds number (i.e., $Re = 104$). This is due to the fact that the system overall global frequency does not change appreciably with the load resistance (see Fig. 5(b)).

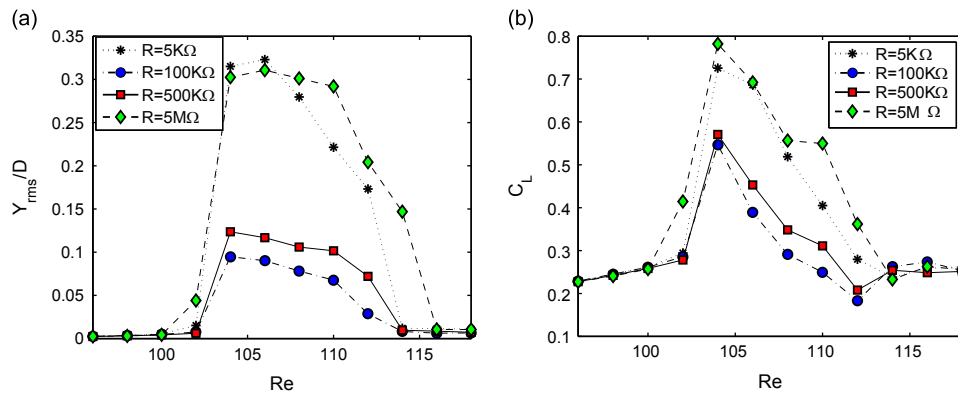


Fig. 8. Variations of the cylinder displacement (Y_{rms}/D) and lift coefficient (C_L) with the Reynolds number for different load resistances: (a) cylinder's displacement, (b) lift coefficient.

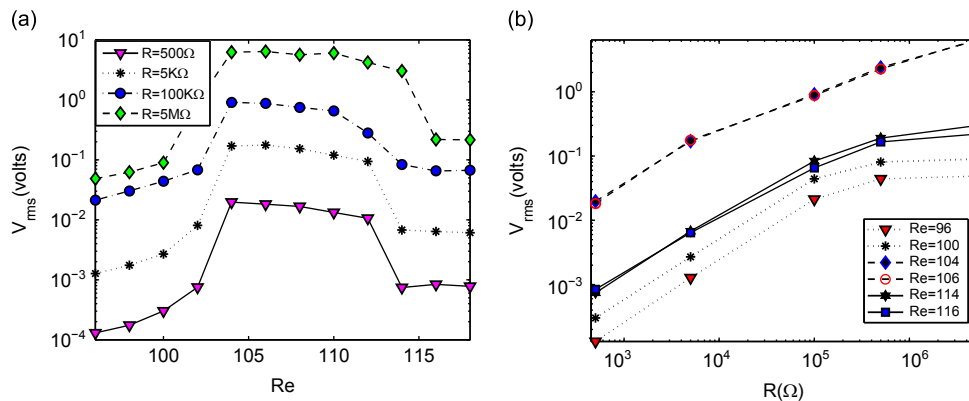


Fig. 9. Variations of the voltage output with the (a) Reynolds number and (b) load resistance.

However, it is important to note that the synchronized amplitude of the cylinder oscillations varies significantly with the load resistance. The amplitude of oscillations is high for small values of the load resistance with a maximum value of $Y_{rms}/D = 0.3229$ for $R = 5 \text{ k}\Omega$. This amplitude decreases to 0.0901 for $R = 100 \text{ k}\Omega$ and increases again to 0.3107 for $R = 5 \text{ M}\Omega$. For $R = 100 \text{ k}\Omega$, the amplitude of cylinder oscillations is the smallest ones compared to the rest of the considered load resistances. This is due to the fact that maximum value of the coupled electromechanical damping is obtained at this load resistance, as shown in the linear analysis performed in Section 4 (see Fig. 5(a)). Variations of the rms fluctuating lift coefficient with the Reynolds number and load resistances are shown in Fig. 8(b). The plot shows that the behavior of the lift coefficient is qualitatively similar to that of the cylinder oscillation amplitude. In fact, smaller values of the fluctuating lift coefficient are obtained for $R = 100 \text{ k}\Omega$ and $R = 500 \text{ k}\Omega$. On the other hand, we note the possibility of antiresonance occurring after the resonance peak in terms of Reynolds number for load resistance values equal to $100 \text{ k}\Omega$, $500 \text{ k}\Omega$ and $5 \text{ M}\Omega$.

Variations of the root mean square values of the voltage with the Reynolds number for different values of the electrical load resistance are shown in Fig. 9(a). This figure shows that, for all considered load resistances, the voltage output increases as the electrical load resistance increases. The maximum voltage is attained when the Reynolds number reaches $Re = 104$. Above this Reynolds number, the voltage remains almost constant over the whole synchronization regime. It is also interesting to note that, by increasing the load resistance, the synchronization regime is slightly expanded to cover higher Reynolds numbers. For example, for the load resistance $R = 500 \Omega$, synchronization starts at the critical value $Re = 104$ and extends to $Re = 112$. In contrast, for $R = 5 \text{ M}\Omega$, synchronization starts at the same critical value $Re = 104$ but extends to $Re = 114$. At $Re = 116$, the voltage is low. Still, the voltage in this regime (post-synchronous regime) is relatively higher in comparison to that in the pre-synchronous regime. This behavior is clearly shown in Fig. 9(b), where the rms values of the voltage are plotted as a function of the load resistance. In this figure, the voltage output is plotted for the pre-synchronous, synchronous, and post-synchronous regimes. For the sake of discussion, we plot only two values from each regime for all considered resistances. Fig. 9(b) shows that the generated voltages at the Reynolds numbers $Re = 96$ and $Re = 100$, which are part of the pre-synchronous regime, are smaller than the corresponding values in the post-synchronous regime (i.e., $Re = 114$ and 116) for all load resistances. However, the voltage output is the largest in the synchronous regime (i.e., $Re = 104$ and 106). Fig. 9(b) also shows that the voltage is larger at higher values of the load resistance. However, the rate of increase is smaller

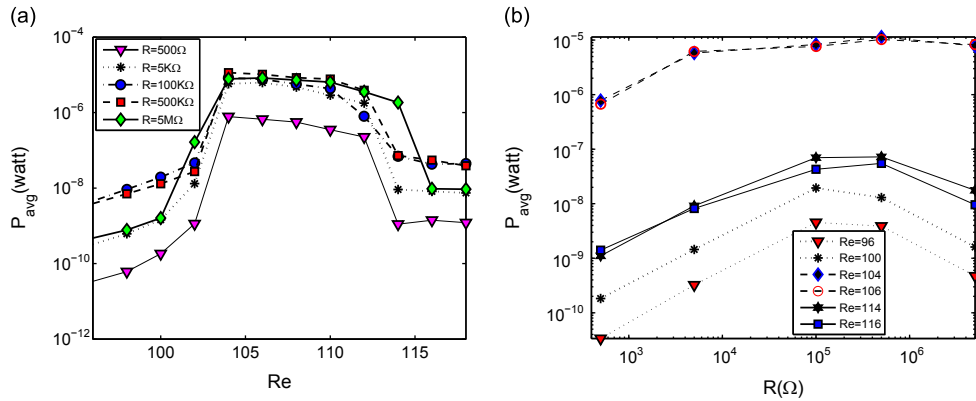


Fig. 10. Variations of the harvested power with the (a) Reynolds number and (b) load resistance.

for $R \geq 500 \text{ k}\Omega$. Similar observations have been made in the literature of piezoelectric energy harvesting from ambient vibrations (based on cantilever beams) [45] and from aeroelastic vibrations (based on wings) [18].

Fig. 10(a) shows variations of the harvested power with the Reynolds number for different values of the electrical load resistance. The generated power is computed from the voltage according to the following relation:

$$P_{\text{avg}} = \frac{V_{\text{rms}}^2}{R} \quad (27)$$

where V_{rms} is the rms value of the voltage output and R is the electrical load resistance across the piezoceramic layer. Fig. 10(a) shows that the highest levels of harvested power are obtained in the synchronization region for all considered load resistances. However, unlike the voltage output, the harvested power achieves a maximum and then decreases when using higher load resistances. This behavior is clear from Fig. 10(b), where the harvested power is plotted as a function of the load resistance. The plot shows that the harvested power increases as the electrical load increases from $R = 500 \Omega$ to $R = 100 \text{ k}\Omega$. When the value of the load resistance is set equal to $R = 500 \text{ k}\Omega$, the harvested power starts to decrease. Here, the maximum power is harvested at $R = 500 \text{ k}\Omega$. Of interest, however, is the fact that, for this optimum resistance, the electromechanical damping is also maximum (see Fig. 5(a)) due to shunt damping effect, this translates into lower amplitudes of the cylinder oscillations (see Fig. 8(b)). This means that the largest oscillations do not lead to maximum generated power, as one would expect from a non-coupled analysis. The existence of an optimum value for the load resistance for which the highest levels of harvested power are obtained has been observed in the literature of piezoelectric energy harvesting from ambient vibrations (based on cantilever beams) [46,47] and from aeroelastic vibrations (based on wings) [18,20].

6. Conclusions

We investigated in detail the concept of energy harvesting from vortex-induced vibrations of a circular cylinder. We solved simultaneously in the time domain for the motions of the cylinder, piezoelectric transducer, and flow using a parallelized computer solver. The simulations were performed for a range of Reynolds numbers that covers the pre-synchronization, synchronization, and post-synchronization regimes. The effect of the load resistance on the harvester response has been analyzed. Based on the linear analysis, we have found that the load resistance impacts the onset of synchronization because it affects the global frequency and damping of the electromechanical system. The results also show that the voltage output continuously increases when increasing the load resistance. In contrast, there is an optimum value of the electrical load resistance for which the level of the harvested power is maximum. This value corresponds to the minimum value of the cylinder's displacement which shows that the electrical and mechanical components of the system are tightly coupled.

Acknowledgment

A. Mehmood gratefully acknowledges the University of Engineering & Technology (UET) Peshawar, Pakistan, for the financial support during his graduate studies. The numerical simulations were performed on the Virginia Tech Advanced Research Computing - System X. The allocation grant and support provided by the staff are also gratefully acknowledged.

References

- [1] P. Murali, Ferroelectric thin films for micro-sensors and actuators: a review, *Journal of Micromechanics and Microengineering* 10 (2000) 136–146.
- [2] W. Zhou, W.H. Liao, W.J. Li, Analysis design of a self-powered piezoelectric microaccelerometer, *Proceedings of the Smart Structures and Materials Conference; Proceedings of SPIE*, Vol. 5763, 2005, pp. 233–240.

- [3] D.J. Inman, B.L. Grisso, Towards autonomous sensing, *Proceedings of the Smart Structures and Materials Conference; Proceedings of SPIE*, Vol. 6174, 2006, p. 61740T.
- [4] J.M. Renno, M.F. Daqaq, D.J. Inman, On the optimal energy harvesting from a vibration source, *Journal of Sound and Vibration* 320 (2009) 386–405.
- [5] S. Roundy, P.K. Wright, A piezoelectric vibration based generator for wireless electronics, *Smart Materials and Structures* 13 (2004) 1131–1142.
- [6] I.D. Capel, H.M. Dorrell, E.P. Spencer, M.W. Davis, The amelioration of the suffering associated with spinal cord injury with subperception transcranial electrical stimulation, *Spinal Cord* 41 (2003) 109–117.
- [7] S. Priya, D. Popa, F. Lewis, Energy efficient mobile wireless sensor networks, *Proceedings of the ASME International Mechanical Engineering Congress Exposition*, Chicago, IL, 2006, pp. 491–498.
- [8] D. Arnold, Review of microscale magnetic power generation, *IEEE Transactions on Magnetics* 43 (2007) 3940–3951.
- [9] P.D. Mitcheson, P. Miao, B.H. Start, E.M. Yeatman, A.S. Holmes, T.C. Green, MEMS electrostatic micro-power generator for low frequency operation, *Sensors Actuators A* 115 (2004) 523–529.
- [10] S.R. Anton, H.A. Sodano, A review of power harvesting using piezoelectric materials (2003–2006), *Smart Materials and Structures* 16 (2007) R1–R21.
- [11] K.A. Cook-Chennault, N. Thambi, A.M. Sastry, Powering MEMS portable devices—a review of non-regenerative and regenerative power supply systems with emphasis on piezoelectric energy harvesting systems, *Smart Materials and Structures* 17 (2008) 043001.
- [12] M.A. Karami, D.J. Inman, Analytical modeling and experimental verification of the vibrations of the zigzag microstructure for energy harvesting, *Journal of Vibration and Acoustics* 133 (2011) 011002.
- [13] R. Masana, M.F. Daqaq, Electromechanical modeling and nonlinear analysis of axially loaded energy harvesters, *Journal of Vibration and Acoustics* 133 (2011) 1–10.
- [14] A. Abdelkefi, A.H. Nayfeh, M.R. Hajj, Global nonlinear distributed-parameter model of parametrically excited piezoelectric energy harvesters, *Nonlinear Dynamics* 67 (2012) 1147–1160.
- [15] A. Abdelkefi, A.H. Nayfeh, M.R. Hajj, Effects of nonlinear piezoelectric coupling on energy harvesters under direct excitation, *Nonlinear Dynamics* 67 (2012) 1221–1232.
- [16] M.F. Daqaq, On intentional introduction of stiffness nonlinearities for energy harvesting under white Gaussian excitations, *Nonlinear Dynamics* 69 (2012) 1063–1079.
- [17] M. Bryant, E. Garcia, Energy harvesting: a key to wireless sensor nodes, *Proceedings of the SPIE* 7493 (2009) 74931W.
- [18] A. Abdelkefi, A.H. Nayfeh, M.R. Hajj, Modeling and analysis of piezoaeroelastic energy harvesters, *Nonlinear Dynamics* 67 (2011) 925–939.
- [19] A. Abdelkefi, A.H. Nayfeh, M.R. Hajj, Design of piezoaeroelastic energy harvesters, *Nonlinear Dynamics* 68 (2011) 519–530.
- [20] A. Abdelkefi, A.H. Nayfeh, M.R. Hajj, Enhancement of power harvesting from piezoaeroelastic systems, *Nonlinear Dynamics* 68 (2011) 531–541.
- [21] C. De Marqui, W.G.R. Vieira, A. Erturk, D.J. Inman, Modeling and analysis of piezoelectric energy harvesting from aeroelastic vibrations using the doublet-lattice method, *Journal of Vibration and Acoustics* 133 (2011) 011003.
- [22] A. Abdelkefi, M.R. Hajj, A.H. Nayfeh, Sensitivity analysis of piezoaeroelastic energy harvesters, *Journal of Intelligent Material Systems and Structures* 23 (2012) 1523–1531.
- [23] A. Abdelkefi, Z. Yan, M.R. Hajj, Modeling and nonlinear analysis of piezoelectric energy harvesting from transverse galloping, *Smart Materials and Structures* 22 (2013) 025016.
- [24] A. Abdelkefi, M.R. Hajj, A.H. Nayfeh, Power harvesting from transverse galloping of square cylinder, *Nonlinear Dynamics* 70 (2012) 1377–1388.
- [25] H.D. Akaydin, N. Elvin, Y. Andreopoulos, Energy harvesting from highly unsteady fluid flows using piezoelectric materials, *Journal of Intelligent Material Systems and Structures* 21 (2010) 1263–1278.
- [26] A. Abdelkefi, M.R. Hajj, A.H. Nayfeh, Phenomena and modeling of piezoelectric energy harvesting from freely oscillating cylinders, *Nonlinear Dynamics* 70 (2012) 1355–1363.
- [27] P.W. Bearman, Vortex shedding from oscillating bluff bodies, *Annual Review of Fluid Mechanics* 16 (1984) 195–1984.
- [28] C.H.K. Williamson, Vortex dynamics in the cylinder wake, *Annual Review of Fluid Mechanics* 28 (1996) 477–539.
- [29] C.H.K. Williamson, R. Govardhan, Vortex-induced vibrations, *Annual Review of Fluid Mechanics* 36 (2004) 413–455.
- [30] R.D. Gabbai, H. Benaroya, An overview of modeling and experiments of vortex-induced vibration of circular cylinder, *Journal of Sound and Vibration* 282 (2005) 575–616.
- [31] R. Mittal, G. Iaccarino, Immersed boundary methods, *Annual Review of Fluid Mechanics* 37 (2005) 199–239–261.
- [32] C.W. Hirt, A.A. Amsden, J.L. Cook, An arbitrary Lagrangian–Eulerian computing method for all flow speeds, *Journal of Computational Physics* 14 (1974) 227–253.
- [33] H.M. Blackburn, R. Henderson, A study of two-dimensional flow past an oscillating cylinder, *Journal of Fluid Mechanics* 385 (1999) 255–286.
- [34] I. Akhtar, Parallel Simulations, Reduced-order Modeling, and Feedback Control of Vortex Shedding using Fluidic Actuators, PhD Dissertation, Virginia Tech, Blacksburg, VA, 2008.
- [35] I. Akhtar, A.H. Nayfeh, C.J. Ribbens, On the stability and extension of reduced-order Galerkin models in incompressible flows: a numerical study of vortex shedding, *Theoretical and Computational Fluid Dynamics* 23 (3) (2009) 213–237.
- [36] I. Akhtar, O.A. Marzouk, A.H. Nayfeh, A van der Pol-duffing oscillator model of hydrodynamic forces on canonical structures, *Journal of Computational Nonlinear Dynamics* 4 (2009) 041006.
- [37] A. Mehmood, A. Abdelkefi, I. Akhtar, A.H. Nayfeh, A. Nuhait, M.R. Hajj, Linear and nonlinear active feedback controls for vortex-induced vibrations of circular cylinders, *Journal of Vibration and Control*, doi: <http://dx.doi.org/10.1177/1077546312469425>, in press.
- [38] M. Ghommam, A. Abdelkefi, A. Nuhait, M.R. Hajj, Aeroelastic analysis and nonlinear dynamics of an elastically mounted wing, *Journal of Sound and Vibration* 331 (2012) 5774–5787.
- [39] B. Carnahan, H.A. Luther, J.O. Wilkes, *Applied Numerical Methods*, John Wiley and Sons, Inc., New York, 1969.
- [40] S. Adhikari, M.I. Friswell, D.J. Inman, Piezoelectric energy harvesting from broadband random vibrations, *Smart Materials and Structures* 18 (2009) 115005.
- [41] S.F. Ali, M.I. Friswell, S. Adhikari, Piezoelectric energy harvesting with parametric uncertainty, *Smart Materials and Structures* 19 (2010) 105010.
- [42] P. Anagnostopoulos, P.W. Bearman, Response characteristics of a vortex-excited cylinder at low Reynolds numbers, *Journal of Fluids and Structures* 6 (1992) 39–50.
- [43] J. Yang, S. Preidikman, E. Balaras, A strongly coupled, embedded-boundary method for fluid–structure interactions of elastically mounted rigid bodies, *Journal of Fluids and Structures* 24 (2008) 167–182.
- [44] K.W. Schulz, Y. Kallinderis, Unsteady flow structure interaction for incompressible flows using deformable hybrid grids, *Journal of Computational Physics* 143 (1998) 569–597.
- [45] A. Erturk, D.J. Inman, A distributed parameter electromechanical model for cantilevered piezoelectric energy harvesters, *Journal of Vibration and Acoustics* 130 (2008) 041002.
- [46] A. Abdelkefi, F. Najjar, A.H. Nayfeh, S. Ben Ayed, An energy harvester using piezoelectric cantilever beams undergoing coupled bending–torsion vibrations, *Smart Materials and Structures* 20 (2011) 115007.
- [47] A. Abdelkefi, A.H. Nayfeh, M.R. Hajj, F. Najjar, Energy harvesting from a multifrequency response of a tuned bending–torsion system, *Smart Materials and Structures* 21 (2012) 075029.